# CFD analysis of natural convection cooling of the in-vessel components during a shutdown of the EU DEMO fusion reactor

# CFD analysis of natural convection cooling of the in-vessel components during a shutdown of the EU DEMO fusion reactor

Andrea Zappatore[1], Antonio Froio[1,*], Gandolfo Alessandro Spagnuolo[2] and Roberto Zanino[1]

[1]*NEMO group, Dipartimento Energia, Politecnico di Torino, 10129 Torino, Italy*
[2]*PPPT Department, EUROfusion Consortium, 85748 Garching bei München, Germany*

In view of the large neutron fluence expected in a fusion power plant, the maintenance of the in-vessel components (IVC) must be carried out using Remote Handling (RH); however, before the RH robots can intervene, the temperature of the IVCs must be reduced, so a cooldown phase is required after the reactor shutdown before maintenance activities can start. In the EU DEMO two options are being investigated to cool down the Breeding Blanket (BB) structures before maintenance, namely introducing fans to pump air in forced convection in the plasma chamber (after opening the Vacuum Vessel), or letting the air at room temperature cool down the structures by natural convection; if the required downtime is acceptable, the second option is clearly preferred, as it would reduce the cost and complexity of the system. This work analyses the natural convection option via a 3D transient Computational Fluid-Dynamics (CFD) conjugate heat transfer model, to evaluate the required time to cool down the BB.

Keywords: DEMO, in-vessel component, natural convection, conjugate heat transfer, CFD, remote handling

## 1. Introduction

The EU DEMO, being developed by the EUROfusion Consortium, is the tokamak fusion reactor aiming to demonstrate the production of electricity (300-500 MW) from fusion power plants in Europe [1]. As the first European device to include a full-scale Breeding Blanket (BB), it will operate as a Component Test Facility for the BB [2], which will then be replaced not only if extraordinary maintenance is needed but also to test different BB concepts, and whenever the BB set will reach the end of life. As the BB first wall directly faces the plasma, the BB will be subject to the largest total neutron fluence and will be activated, requiring a Remote Handling (RH) system to operate on it for maintenance.

Current RH system designs in EUROfusion foresee a temperature limit to operate the RH of 100-150 °C [3], whereas the operating temperature window of the BB is 300÷550 °C during normal operation; in addition, the BB will heat up also after the shutdown, in view of the decay heat generated therein (~1-2 % of the power released during the flat-top immediately after the shutdown [4]). Consequently, after the reactor shutdown, the BB must be cooled down before the first segment can be removed; the BB transporter will extract all BB segments from the upper port [5], see Fig. 1, from which also the BB coolant inlet and outlet pipes are routed [2]. To maximize the plant availability, the downtime caused by the maintenance should be minimized, and consequently, also the time needed to cool down the segments play a role in the plant performance. If an active cooling system is employed, this time can be reduced, however introducing further complexity and cost in the plant; on the other hand, if the Vacuum Vessel (VV) is opened, the BB segments will be passively cooled in natural convection by the air entering at room temperature from the lower port, see Fig. 1.

In the present work, the natural convection cooling strategy is assessed, in order to find the time needed to meet the RH requirement after the reactor has been shut down. To this aim, a 3D transient CFD conjugate heat transfer (CHT) model was developed and applied using the software STAR-CCM+ v. 2019.3 [6]. To the best of the authors' knowledge, this is the first time that a 3D transient thermal-hydraulic model is employed to analyse the cooldown transient of the BB during reactor shutdown; indeed, most of past efforts have been put either in estimating the shutdown dose rate (see e.g. [7][8]), or on pure thermal analyses including radiative and conductive heat transfer only (see e.g. [9][10]). More recently, a CFD analysis of the natural circulation of the helium coolant in the DEMO cryostat following a Loss-of-Coolant Accident has been carried out [11]; however, the work was focused on accidental condition and carried out by means of steady-state simulations only.

## 2. The 3D CFD model

### 2.1 Model equations

The 3D CFD model implemented in STAR-CCM+ enforces the fundamental conservation laws of mass, momentum and energy [12], in both the fluid and solid domains.

author's email: antonio.froio@polito.it

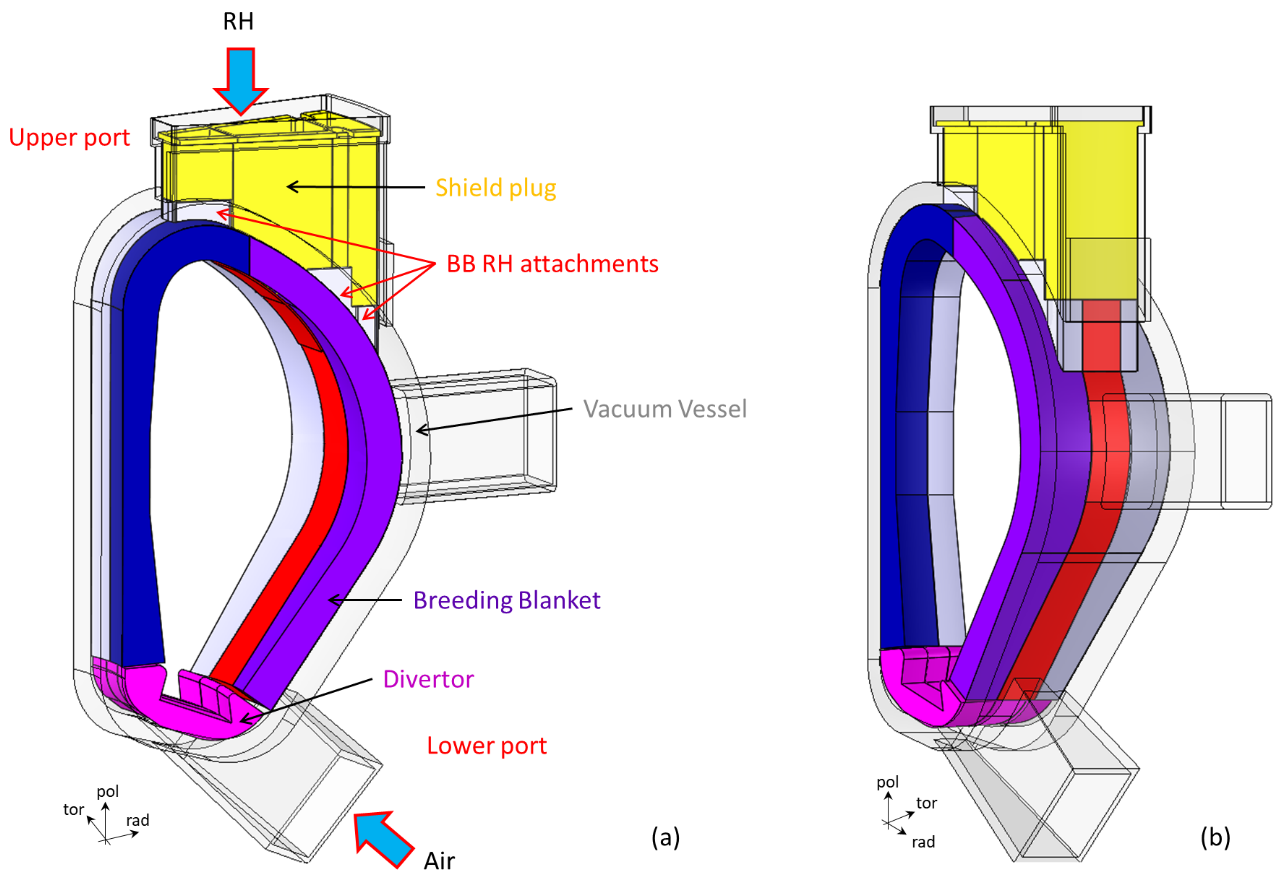


Fig. 1. View of one sector of the EU DEMO, showing the internals (BB, divertor, shield plug), the upper port where the RH operates and the lower port where air enters the VV. The BB attachments for RH operation are also shown.

Both the solid and the fluid are assumed to have constant thermophysical properties (density $\rho$, specific heat $c$, dynamic viscosity $\mu$, thermal conductivity $k$); however, as the driver of fluid motion in natural convection is buoyancy (driven in turn by the density differences), the body force term in the fluid momentum equation $\mathbf{f}_b$ is computed via the Boussineq approximation as

$$\mathbf{f}_b = \rho \mathbf{g} \beta \left(T_{ref} - T\right) \tag{1}$$

where $\mathbf{g}$ is the gravity acceleration, $\beta = 1/T_{ref}$ is the thermal expansion coefficient of the fluid (assumed constant), $T_{ref} = 300$ K is the reference temperature and $T$ is the local fluid temperature.

The conductive heat flux $\mathbf{q}''$ (in both solid and fluid) is computed via Fourier's law of conduction

$$\mathbf{q}'' = -k \nabla T \tag{2}$$

Note that no volumetric heat source $q'''$ is present in the fluid energy equation, whereas its value in the solid domain is a known term, whose value is reported in section 2.4 below.

Under these assumptions, for the fluid domain the three above-mentioned laws correspond to the set of incompressible Navier-Stokes equations:

$$\nabla \cdot \mathbf{v} = 0 \tag{3}$$

$$\frac{\partial(\mathbf{v})}{\partial t} + (\mathbf{v} \cdot \nabla)\mathbf{v} = -\frac{1}{\rho}\nabla p + \nu \nabla^2 \mathbf{v} + \frac{1}{\rho}\mathbf{f}_b \tag{4}$$

$$\begin{aligned} &\rho \frac{\partial E}{\partial t} + \rho(\mathbf{v} \cdot \nabla)E = \\ &= -(\mathbf{v} \cdot \nabla)p + \nabla \cdot (\mathbf{v} \cdot \boldsymbol{\sigma}) + \mathbf{f}_b \cdot \mathbf{v} + k\nabla^2 \mathrm{T} \end{aligned} \tag{5}$$

where $t$ is the time, $\nu = \mu/\rho$ is the kinematic viscosity, $p$ is the pressure, $E = e + \frac{1}{2}|\mathbf{v}|^2$ is the total energy per unit mass, $e$ is the specific internal energy and $\boldsymbol{\sigma}$ is the stress tensor.

Concerning the solid domain, since it has zero velocity (and its mass is not changing), only the energy conservation equation is required. Under the assumptions above, and recalling that the internal energy variation $dE$ can be expressed in terms of temperature variation (via the specific heat definition $dE = c\, dT$), it takes the form

$$\rho c \frac{\partial T}{\partial t} = k \nabla^2 \mathrm{T} + q''' \tag{6}$$

## 2.2 Geometry

The reference geometry assumed in this work is taken from the EU DEMO 2017 baseline [13], [14]; as BB concept the Helium-Cooled Pebble Bed [15] (HCPB) is assumed. A possible application of the present model to the Water-Cooled Lithium Lead [16] (WCLL) concept would be straightforward since the only changes in the model would be the different material properties and heat load, which would affect significantly the transient timing but not the model, solvers, and meshing strategy described here.

The air entering from the lower port will flow in the 2 cm gaps between two adjacent BB segments and between the BB and the VV, see Fig. 2; this dimension is extremely small when compared to the tens of meters of the plasma chamber, so detailed modelling is included only for the sector under maintenance (as maintenance is assumed to be performed one sector at a time [17]). This choice is justified considering that the BB sectors *not* under maintenance will be actively kept at ~300 °C using the helium cooling system [17]; moreover, the shield plug will be removed only from the upper port of the sector under maintenance, so the flow in the gaps in the non-maintained sectors can be considered negligible. In view of this assumption, the domain boundary in the non-maintained sectors is the envelope of the First Wall (FW) and divertor plasma-facing surfaces, see Fig. 3.

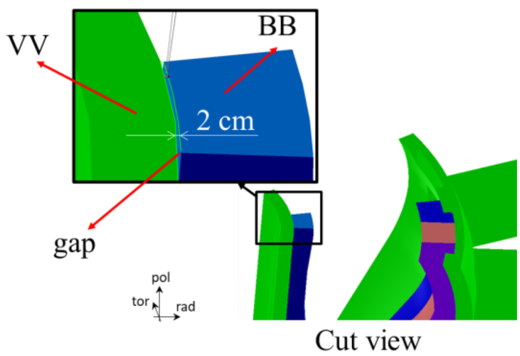


Fig. 2. Cut view of an EU DEMO sector, showing in the inset the gap between BB and VV.

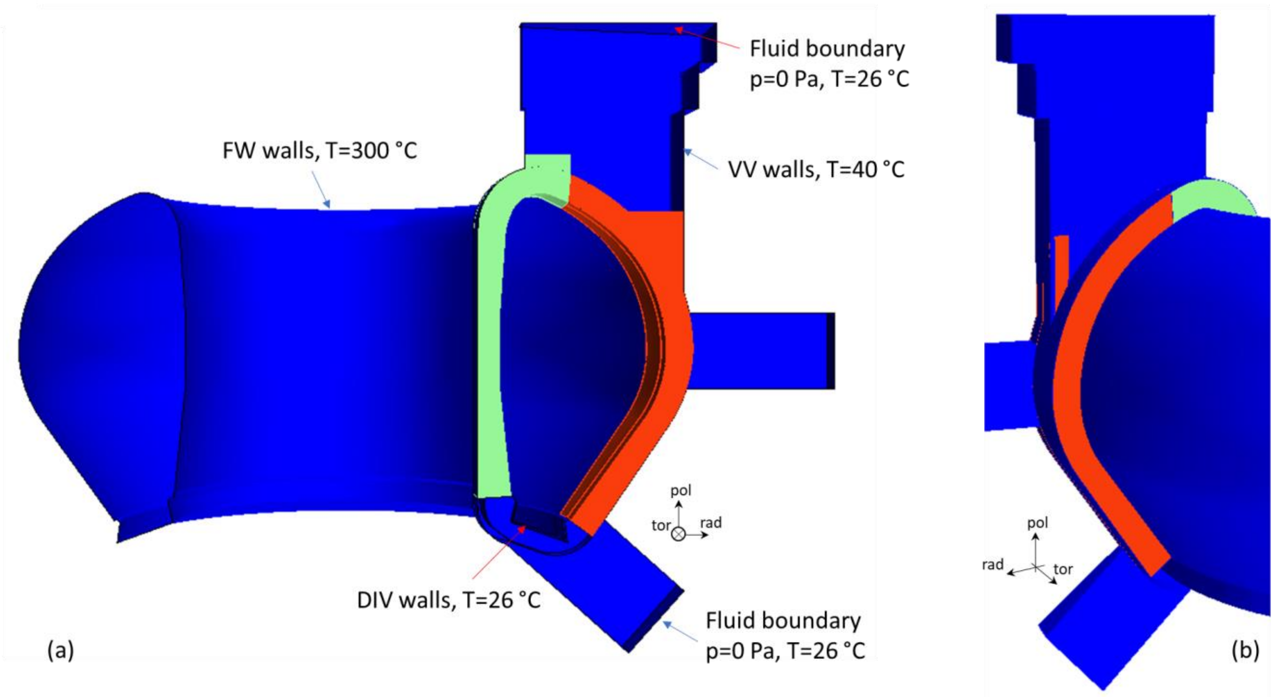


Fig. 3. (a) Computational domain including the BB sector and VV considered for the present analysis. The IB and OB segments are coloured in light green and red, respectively. The solid and fluid boundary conditions are also shown. (b) Rear view of the computational domain.

Finally, just as the BB and VV geometries, also the boundary conditions and thermal driver (see below) are symmetric with respect to a vertical plane which cuts in half the maintained sector; therefore, only half of the tokamak is considered here, cutting it with a vertical plane passing through the vertical midplane of the sector undergoing maintenance; note that this vertical midplane cuts in half the central outboard (OB) segment and the gap between the two inboard (IB) segments, i.e. it belongs to the solid domain on the OB and to the fluid domain on the IB. The computational domain is reported in Fig. 3, where the OB and IB segments are coloured in red and light green, respectively.

The computational domain includes a fluid region (lower port, equatorial port, upper port and VV) and the solid structures of the inboard and outboard segments of one BB sector.

### 2.3 Boundary and initial conditions

The upper and lower ports are assumed to be open and in contact with the environment of the tokamak building, while the equatorial port is assumed to be closed; to simulate environmental conditions, the top surface of the upper port and the bottom surface of the lower port are at fixed pressure (0 Pa gauge) and temperature (assuming ambient conditions, i.e. 26 °C). The air could then, in principle, enter (and exit) from both the upper and the lower port; however, due to stack effect [18], it is expected to flow upwards, and then enter from the lower port and exit from the upper port. On the symmetry surfaces, the normal velocity and the normal gradient of all the other variables are zero. The envelope of the FW, see section 2.2, is set at a constant and uniform temperature equal to 300 °C, since all the other non-maintained sectors are assumed to be kept at that temperature. The same assumption holds for the VV and for the divertor, whose surfaces are then set at 40 °C [19], [20] and 26 °C [19], respectively; radiative heat transfer towards these low-temperature surfaces is conservatively neglected. The boundary conditions are summarized in Fig. 3(a).

As initial conditions, the working fluid (air, modelled as ideal gas) is assumed to be stagnant (zero velocity) and at a pressure of 0 Pa gauge; both the solid and the fluid domain are assumed at 300 °C. This assumption stems from having a relatively long time (1 month, see section 2.4 below), during which air is let in and all the BB surfaces (as well as internals) are actively kept at 300 °C.

### 2.4 Thermal driver

The thermal driver in the transient is represented by the decay heat in the BB. It has been fitted to a continuous function from the data available in [21], see Fig. 4. The best fit equation is

$$\log_{10}\frac{q'''}{q_0} = a(\log_{10} t)^3 + b(\log_{10} t)^2 + c\log_{10} t + d \qquad (7)$$

where $t$ is the time after reactor shutdown in seconds, $q_0 = 256.7\ \mathrm{W/m^3}$ for the IB segments and $q_0 = 216.5\ \mathrm{W/m^3}$ for the OB segments; the fit constants are $a = -0.015713$, $b = 0.108177$, $c = -0.393218$ and $d = 2.28004$.

The start time of the transient is 1 month after shutdown, to take into account the time needed to remove the shield plug and cut the coolant pipes in the upper port, to allow RH operation therein [19]. The heat is assumed to be deposited uniformly in all the OB and IB segments; however, the BB segments in the sectors not undergoing maintenance will have the coolant pipes in place and the cooling system active, which, being designed to withstand the nominal load, will maintain the solid temperature fixed at ~300 °C as discussed above. In the maintained sector, instead, the cooling system will not be active anymore as the coolant pipes will be cut as mentioned above.

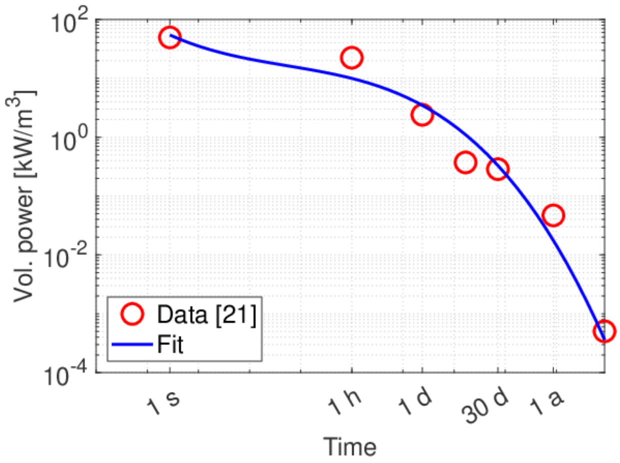


Fig. 4. Time evolution of the decay heat, averaged between inboard and outboard; the circles represent the data taken from [21].

## 3. Space and time scales affecting mesh and solution strategy

The problem at hand is a classical multiscale problem, considering both the space and the time domain. Indeed, as mentioned in section 2.2, the regions where most of the flow will occur are the 2 cm thick gaps at the top and bottom of the segments, where the whole mass flow rate will be forced to flow, and the largest speeds (and velocity gradients) are expected; on the other hand, the vertical dimension of the segments is ~10 m and the domain length in the toroidal direction is ~30 m. Considering also that in the plasma chamber region, and in particular far from the sector undergoing maintenance, the velocities are expected to be much lower than in the gaps, a strongly non-uniform mesh is generated in the fluid region.

More in detail, an unstructured, conformal, polyhedral mesh is used in the solid and fluid regions, except for the gaps, where a structured, conformal, hexahedral mesh is adopted, to resolve the fluid flow without increasing dramatically the cell count (the grid independence study for the mesh in the gap region is reported in the Appendix A). A detailed view of the mesh adopted in this work is available in Fig. 5; the overall cell count is ~4×10$^5$ cells, ~90 % of which are in the sector undergoing maintenance.

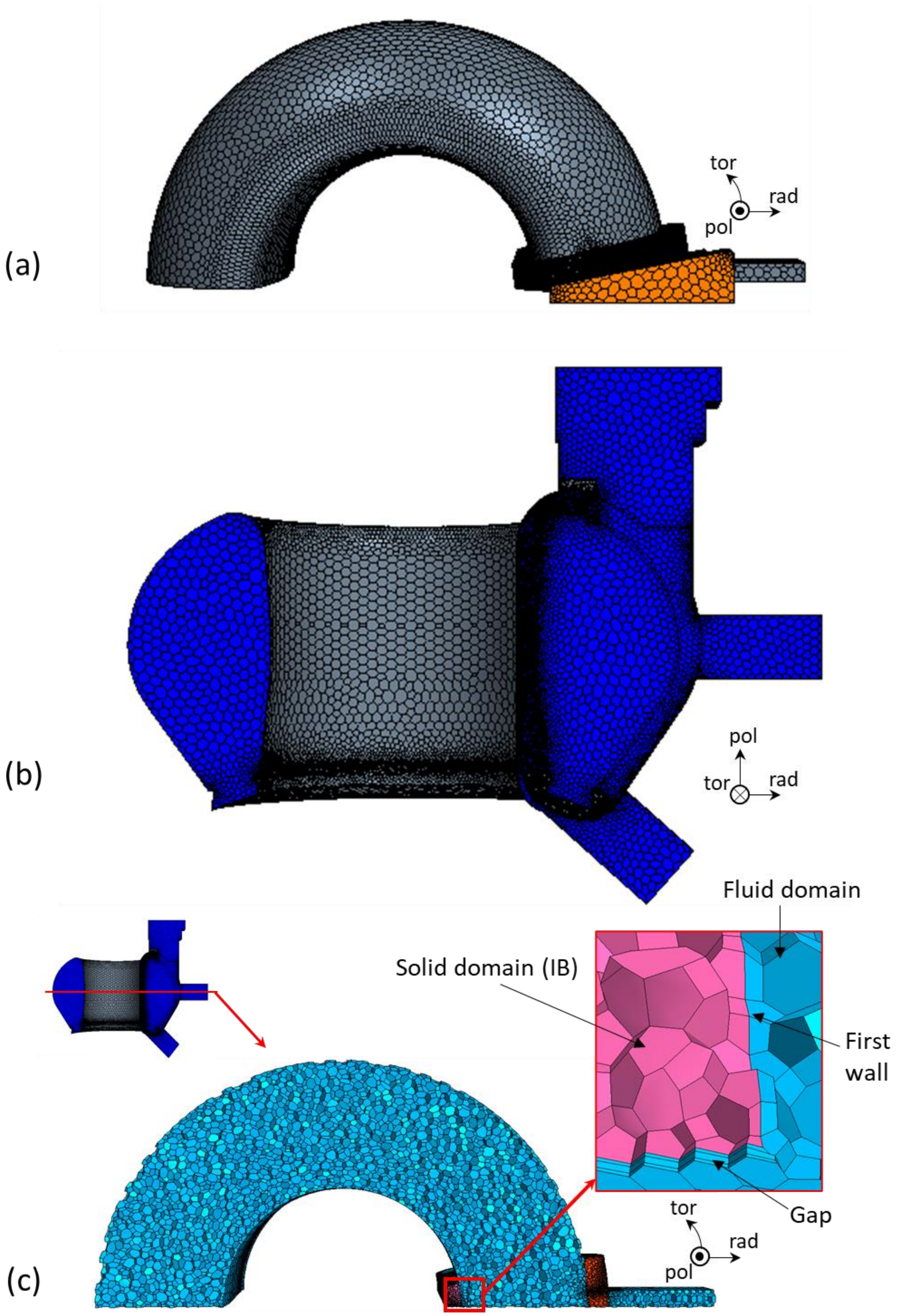


Fig. 5. Top view (a), poloidal cross-section and front view (b) and horizontal cross-section (c) of the mesh adopted for this work. The surfaces are coloured according to the type of fluid boundary condition: blue = symmetry plane, grey = wall and orange = pressure outlet. In (c) a zoom shows the layered mesh in the fluid domain in the gaps between adjacent segments and a much coarser mesh in the remaining solid and fluid regions.

Concerning the time scales,

- the advective time scale can be estimated as $L_f/v$ (where $L_f \sim 9$ m is the height of the chamber and $v \sim 6$ m/s[1]), yielding ~1 s,
- the convection time scale is ~$10^5$ s; it can be estimated as $\rho c V/(HTC \cdot A)$ where $V$ is the solid volume (see Appendix B), respectively, $HTC \sim 4$ W/(m$^2$ K) (estimated in Appendix A) is the heat transfer coefficient and $A$ is the heat transfer area,
- the conduction time scale is also ~$10^5$ s and can be estimated computed as $L_s^2/\alpha$, where $L_s = V/A \sim 2$ m is the solid characteristic length and $\alpha = k/\rho c$ is the solid thermal diffusivity (see Appendix B).

As a consequence, the fluid solver in principle requires a much shorter time step with respect to the solid solver, i.e. if the two solver are run in a fully-coupled fashion, the solid solver is called unnecessarily often to keep the pace of the fluid solver (which is the bottleneck due to the shorter time scale and to the larger complexity of the model, see section 2.1 above).

To speed up the solution of the transient CHT problem, we adopt a partially decoupled approach: the fluid solver works with a time step $\Delta t_{fluid} = 0.2$ s and the solid solver with a time step $\Delta t_{solid} = 1$ s. The two solvers proceed in series, synchronising them periodically (every $\Delta t_{solid}$), i.e. exchanging the required information according to the scheme in Fig. 6: at each solid time step, the solid solver provides the fluid solver with the solid (surface) temperature; the fluid solver, after 5 time steps, provides back the solid solver with the fluid temperature and heat transfer coefficient. These operations are automatically repeated by the software until the transient is finished. Considering also that the solution of the heat diffusion problem is very fast (requiring usually one iteration per time step to converge), thanks to this approach, the time required for the simulation is nearly identical to that required by a pure fluid simulation.

The space and time convergence studies are reported in the 0.

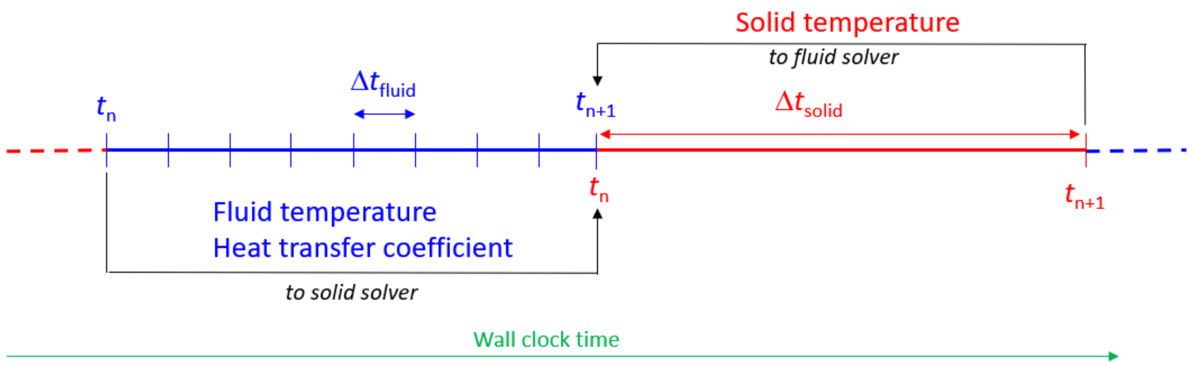


Fig. 6. Coupling strategy between fluid and solid solvers; the exchanged information is also reported. Note that the wall clock time (green arrow) needed to solve each Δt is not to scale.

## 4. Models and solvers

In order to choose the most appropriate models and solvers, the flow regime is assessed estimating the Rayleigh number $Ra$ according to

$$Ra = \frac{g\beta(T_s - T_\infty)\delta^3}{\nu\alpha} \quad (8)$$

which is valid when the solid surface temperature $T_s$ is imposed; here $T_\infty$ is the fluid bulk temperature and $\delta$ is the gap thickness. Since the temperature difference at the numerator will decrease with time, $Ra$ is computed at the beginning of the transient to have an upper bound. In our case, considering $T_s = 300$ °C and $T_\infty = 26$ °C, $Ra \cong 3 \cdot 10^5$; as $Ra < 10^9$, the flow regime will be laminar [22]. This assumption has been verified a posteriori, computing $Ra$ from the simulation results: indeed, in the entire domain, and during the entire transient, the computer $Ra$ is always $< 2 \cdot 10^5$.

A coupled solver for the set of laminar Navier-Stokes equations plus the energy conservation equation is used, according to [23], as the momentum equation driver is the buoyancy term, which depends on the temperature field; as $\beta(T_s - T_\infty) < 1$, the Boussinesq approximation is used to treat the temperature dependency of the density [22], see also section 2.1 above.

These choices have been validated against a simple case (see Appendix A). The material properties used in

[1] The velocity has been estimated from the stack effect relation $v = C\sqrt{2gh\frac{T_i - T_o}{T_i}}$ [18], where $C$ is the discharge coefficient, $g$ is the gravity acceleration, $h$ is the stack height, $T_i$ and $T_o$ are the warm and cold temperatures. In the case at hand, $C = 0.65$, $h = 9$ m, $T_i = 300$ °C and $T_o = 26$ °C.

this work are reported in the Appendix B. The simulation file is available in [24].

## 5. Results

A simple lumped (0D) analysis, see the equation below, estimates that ~21 days are needed to reach 150 °C on average in the segments;

$$\rho c_p V \frac{dT}{dt} = q'''V + hA_w(T_f - T) \quad (9)$$

In (9), $\rho$ and $c_p$ are the *average* density and specific heat of the segments, respectively, see Appendix B, $V$ is the total volume of the segments, $T$ is the average temperature of the segments, $q'''$ is the volumetric heat generation, see section 2.4, $h$ is the heat transfer coefficient computed according to (12), $A_w$ is the wetted surface (to be consistent with (8), only the surfaces exposed to the gaps have been considered, leading to $A_w$ = 88 m$^2$) and $T_f$ is the fluid temperature, assumed constant and equal to 26 °C. The temperature evolution, as computed with the lumped model, is reported in Fig. 7.

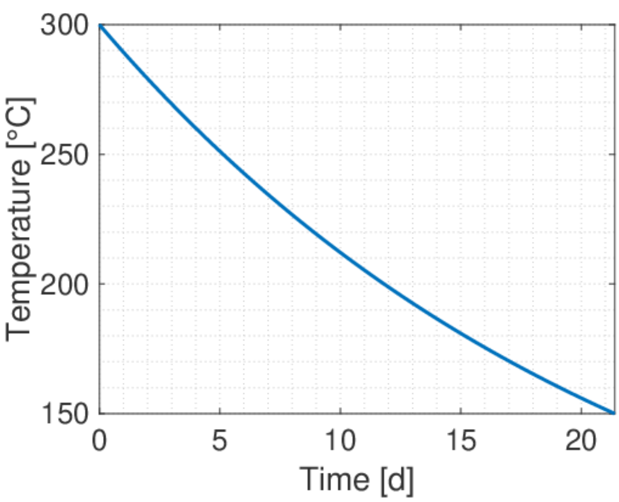


Fig. 7. Time evolution of the temperature in the BB segments, as computed with the lumped (0D) model.

This 0D analysis is however only a rough and especially non-conservative estimate of the expected transient duration, which will necessarily be longer as 1) the temperature of interest is local rather than average and 2) the surrounding walls are kept at high temperature (300 °C), which will also heat up the fluid.

Fig. 8 reports the temperature field on the symmetry plane of the maintained sector, which cuts the gap between the two IB segments and the central OB segment, at different times throughout the transient. As fresh air enters the VV mainly from the lower port (due to natural circulation, see also the discussion below), the BB segments tend to cool down from the bottom part, which is non-optimal as the RH system will intervene from the top, that remains hotter for the entire transient duration. Moreover, the figure shows that heating of the BB segments, both IB and OB, because of the decay heat, lasts ~6 hours only. After that, the bottom part reaches an acceptable temperature after ~2 days, whereas the top of both segments cools down in a much longer time; this result is driven by the long conduction time scale identified above (~10$^5$ s, i.e. ~2 d), as well as by the complex path the fresh air has to follow to reach it.

Fig. 9 reports the evolution of the maximum and average solid and fluid temperatures, as well as the temperature evolution as computed with the 0D model; in the 3D model, the average solid temperature is obtained as the volume-averaged value in all the BB segments (both IB and OB), and the average fluid temperature is obtained as the volume-averaged value in the entire fluid domain. The initial increase phase is indeed negligible (lasting ~6 h and reaching a maximum value ~301 °C), due to the low value of the decay heat. The maximum temperature decreases then with an exponential trend, reaching the RH system threshold after ~15 d on the OB and ~85 d on the IB. Note that, in order to let the temperature decrease by few °C as the solid temperature gets closer to that of the fluid, it takes several weeks, i.e. 65 days are needed to go from 170 °C to 150 °C maximum temperature at the IB. As can be seen from Fig. 9(b), the asymptotic temperature to which the solid tends is ~100 °C, i.e. the average fluid temperature. The key aspect is that such asymptotic behavior of the OB temperature starts after the target temperature has been reached and thus does not affect the RH operation start time, whereas for the IB it starts when the maximum temperature is ~20 °C above the threshold, causing the transient time to increase significantly. A possible mitigation action could then be to slightly enlarge the operation window of the RH system: for instance, an increase of 10 °C (from 150 °C to 160 °C) would reduce the cooldown time to ~30 d, whereas increasing to 170 °C would allow operating after 20 d. Nevertheless, as the OB segments will be removed first [5], RH operations may start when the OB is sufficiently cool, leaving the IB more time to cool down.

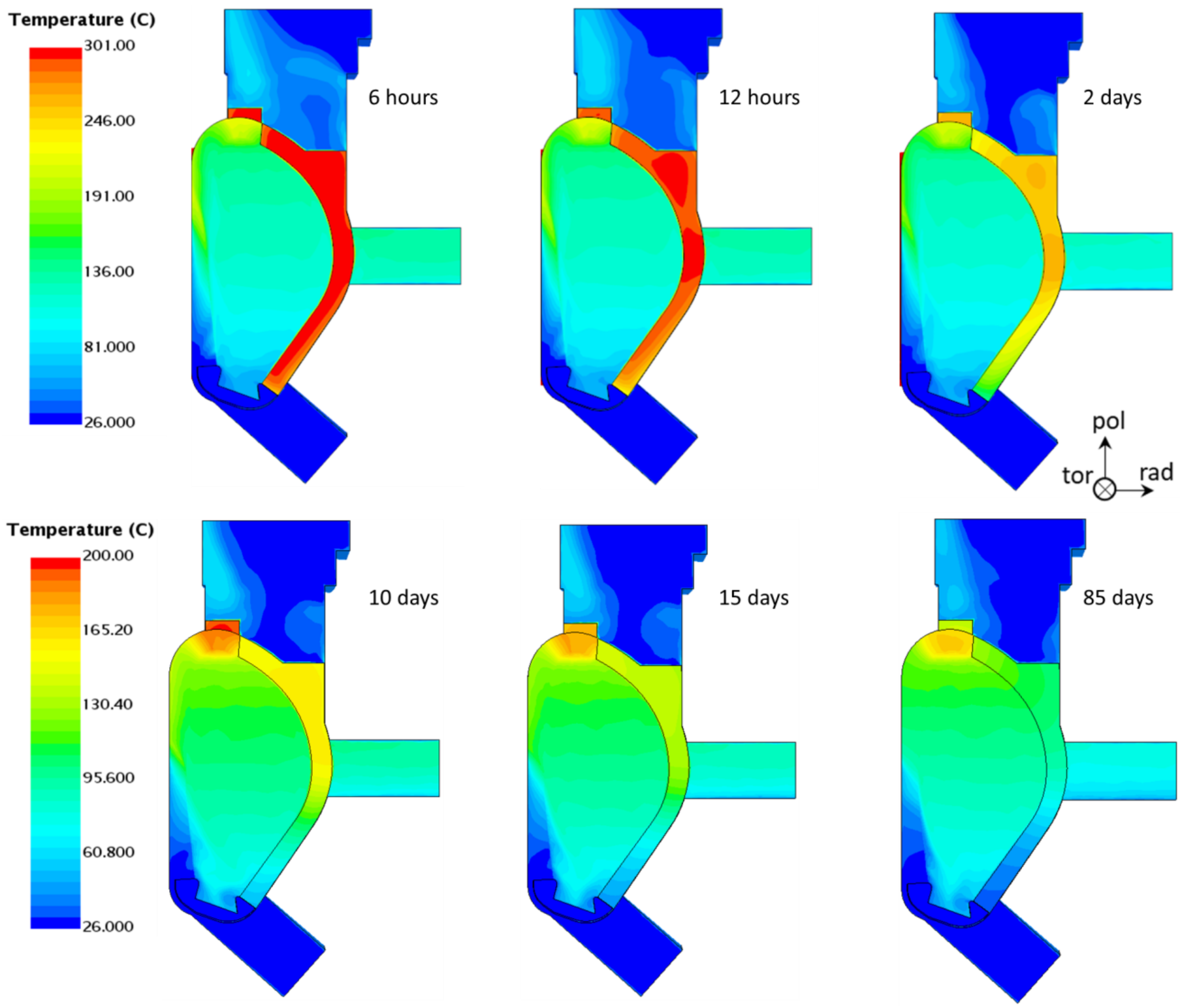


Fig. 8. Temperature field on the symmetry plane of the maintained sector at different times; note that on the second row of the figure, the temperature scale is different, to better appreciate the temperature distribution.

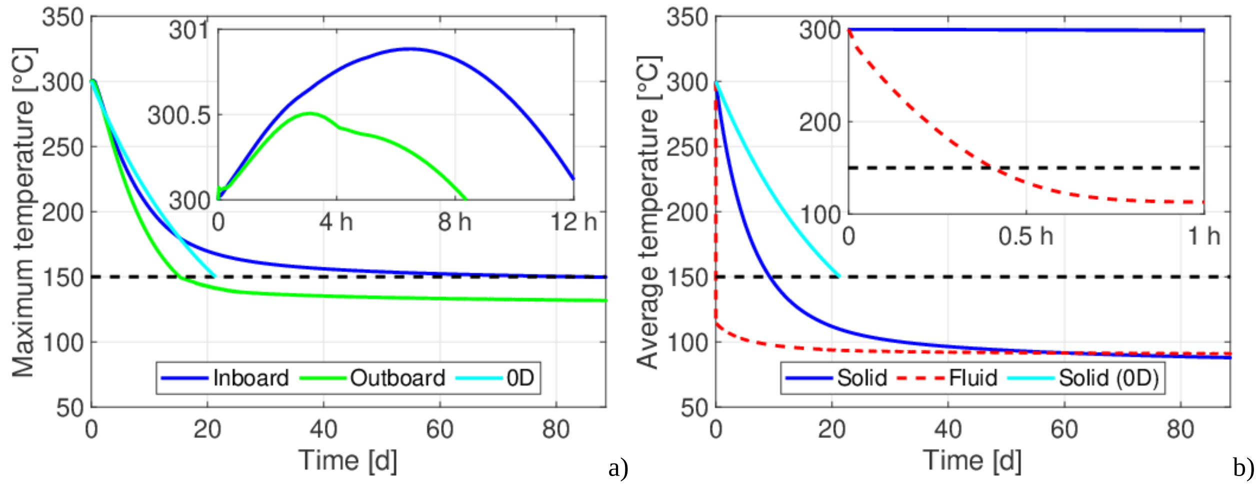


Fig. 9. Evolution of (a) maximum solid temperature and (b) average temperature in the solid and fluid domains; the solid temperature evolution computed with the 0D model is also reported. The dashed black line represents the 150 °C threshold. The insets show the zoom in the first 12 h (a) and 1 h (b). The 0D temperature is not visible in the insets as it is monotonically decreasing in (a) and totally overlapping with the 3D solid line in (b).

The velocity field after 3 days from the initiation of the transient is reported in Fig. 10. The fluid enters the VV from the lower port, as in the upper port region the flow is mainly outwards, see Fig. 10. This behaviour meets the expectations of a natural circulation flow, where the air, heated up by the contact with the hot chamber walls, flows upwards having a lower density. In the bottom region, most of the entering mass flow rate flows towards the IB, since a larger gap between the divertor and VV walls is present with respect to the OB side, see the insets in Fig. 10. This rising mass flow rate of fresh air splits in the several gaps present in the lower part of the chamber, see Fig. 11: the main flow (indicated with "A") splits in:

- B: rising flow along the gap between the back of the IB segments and the VV walls;
- C: flow in the gap between adjacent divertor cassettes;
- D: flow in the gap between the two IB segments. Note that in Fig. 10 the symmetry plane cuts in half this gap. In addition, since the entering mass flow rate must flow through a much smaller cross-section, it accelerates, as it can be noticed in Fig. 10;
- E: the flow in the gap between the IB segments and the divertor cassettes.

Except for "B", all the other contributions flow towards the plasma chamber. However, most of the fluid rises along the gap rather than flowing inside the plasma chamber (see Fig. 10), as the flow driver is the density (temperature) difference, which is maximum close to the chamber surface; the fluid which enters the plasma chamber slows down and shows some low-velocity vortices. The air flows outside of the plasma chamber inside the upper port region from the gap between the IB and OB segments. At this point, however, the fluid has already heated up significantly (see Fig. 8), so the cooling of the top portion of the BB is less effective. Therefore, if a faster cooling is required than foreseen in Fig. 9, an active cooling system will be needed, which would also allow cooling first the top part of the segment, thus significantly reducing the unavailability; on the other hand, cooling (actively) the BB from the top would be counterposed by the natural convection, so an additional (parametric) analysis is envisaged, to assess how beneficial forced convection could be. Another possible solution, which could be further investigated in the future, is the possibility to cool down the BB segments to a lower temperature than 300 °C prior to disconnecting the primary coolant system.

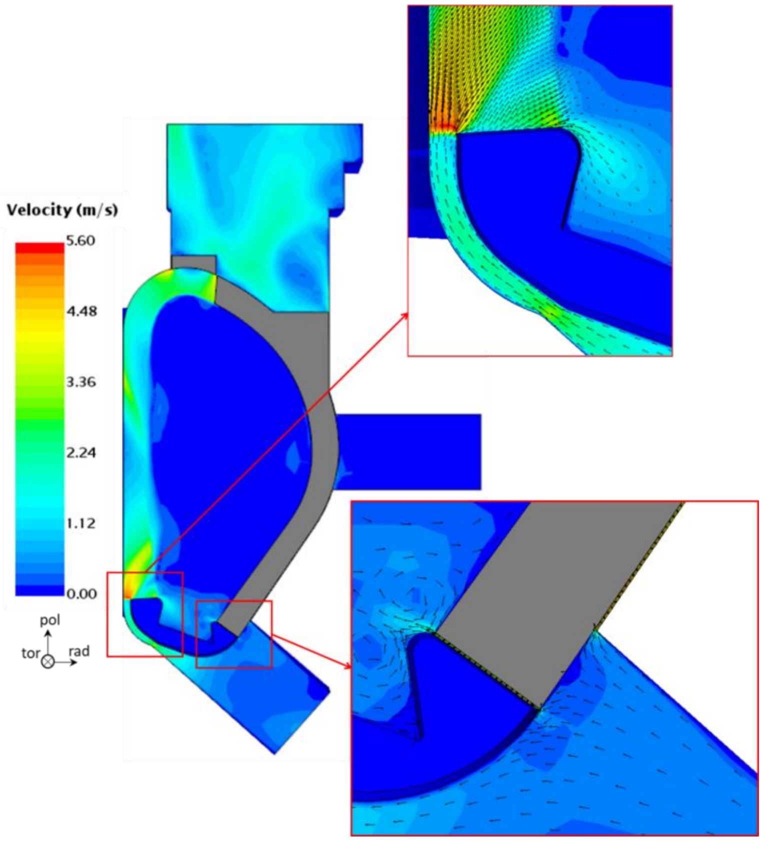


Fig. 10. Velocity magnitude and vector field on the symmetry plane of the maintained sector, 3 days after the beginning of the transient; the insets report the detail of the flow field at the bottom of the IB and OB segments.

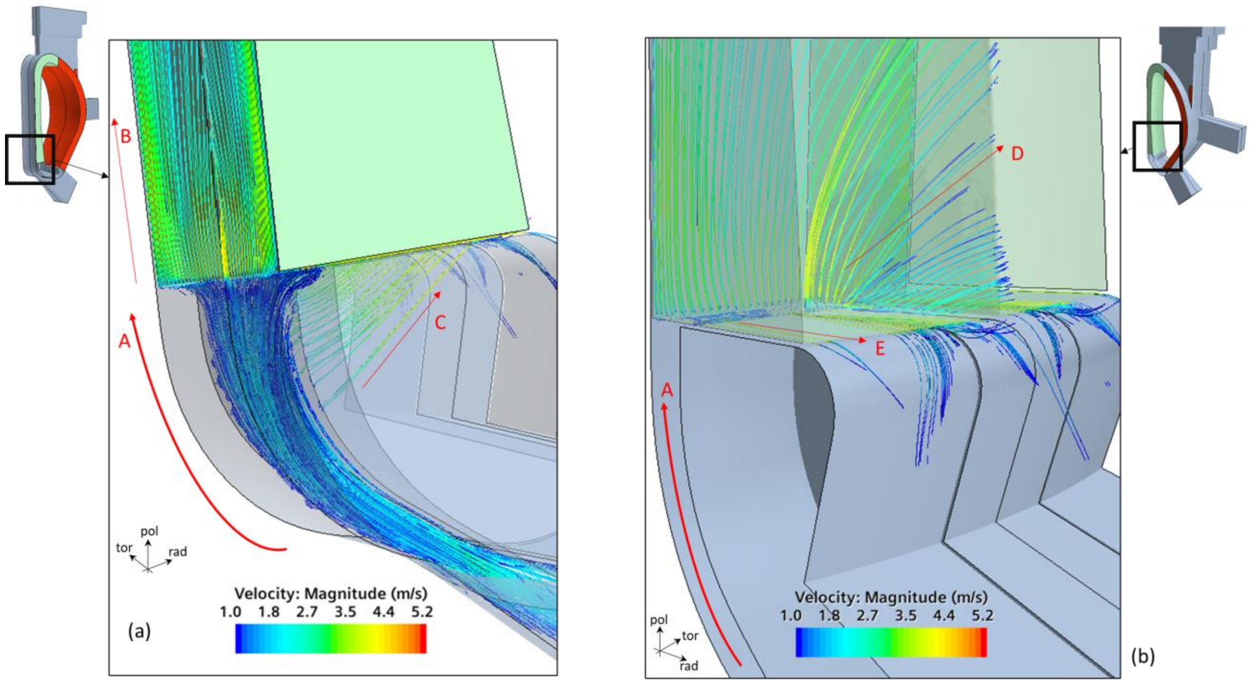


Fig. 11. Streamlines after 9 days from the beginning of the transient in the (a) region between the divertor cassettes and VV walls and in the (b) bottom region of the IB segments and divertor cassettes facing the plasma chamber. A: main flow from the lower port towards IB; B: flow between the back of the IB segments and the VV walls; C: flow between adjacent divertor cassettes; D: flow between adjacent IB segments; E: flow between IB segments and divertor cassettes.

Concerning the (local) heat transfer coefficient $HTC_{local}^{comp}$, it is computed according to

$$HTC_{local}^{comp} = \frac{q_s''}{(T_s - T_{ref,in})} \tag{10}$$

where $q_s''$ is the surface heat flux, $T_s$ is the surface temperature and $T_{ref,in}$ is a reference temperature, assumed equal to the inlet temperature.

$HTC_{local}^{comp}$ confirms the behavior discussed above. The fluid travels with larger velocities close to the bottom part of the segments, thus leading to larger heat transfer coefficients in that region, see Fig. 12. On the contrary, the surfaces facing the plasma chamber are characterized by low, i.e. very close to zero, heat transfer coefficient, because the fluid is almost stagnant there. Furthermore, during the transient, the thermal driver becomes less strong (because the segments cool down, thus the temperature difference between the solids and the fluid is smaller), so the average velocity of the fluid is lower. This has an impact on the heat transfer coefficient, which becomes lower and lower throughout the transient, see Fig. 12. Indeed, the average heat transfer coefficient (weighted on the wetted surfaces) is equal to 2.4 W/(m² K) and to 1.8 W/(m² K) after 6 hours and 10 days from the beginning of the transient, respectively. Note that these average values are in line with the rough estimation obtained with available correlations, see Appendix A.

Finally, it is important to highlight that the time computed to reach 150 °C on both IB and OB segments is, in some sense, conservative, since the radiative heat transfer towards the VV (and, to a lesser extent, divertor) surfaces at low temperatures would help to reduce the BB temperature and has been neglected in this work.

## 6. Conclusions and perspective

A 3D transient CFD model has been developed to analyse the CHT problem of natural convection cooling of a sector of the HCPB BB in the EU DEMO tokamak, investigating the time needed, starting 1 month after reactor shutdown, to cool down the BB until the RH system requirements are met. A detailed model of the sector under maintenance has been included, with a refined mesh in the small gaps between the BB segments and the VV. All the other sectors have been included, to take into account also the flow of air towards the non-maintained sectors.

The model results show that, assuming the start of the transient 1 month after the reactor shutdown, ~15 days are needed to cool the top of the OB segments and ~85 days for the IB segments; considering that the OB segments will be removed first, RH operation could, however, start after 15 days.

In perspective, the model will be applied to analyse the effect of an active cooling system intervening from the upper port, which should reduce significantly the time needed to meet the RH requirements by cooling faster (in forced convection) the top region of the BB, where the RH will be attached to handle the segments. Also, the possibility to actively cool down the segments before starting the transient will be investigated. In addition, it should be interesting to perform a similar analysis for the Water-Cooled Lithium-Lead BB concept, which, having a different material composition, may be characterized by much different time scales.

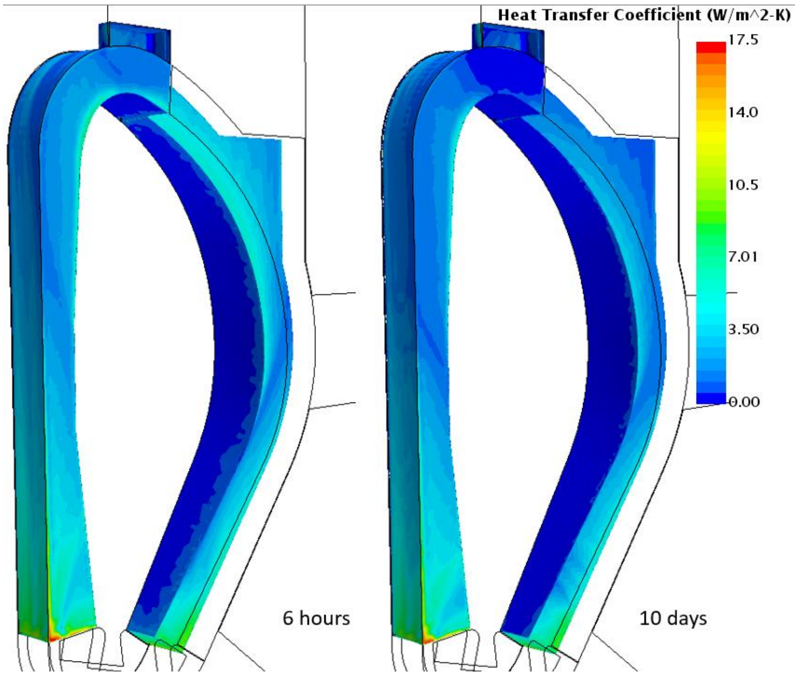


Fig. 12. Distribution of the heat transfer coefficient on the surfaces of one IB and one OB segment after 6 hours and 10 days from the beginning of the transient.


## Acknowledgements

This work has been carried out within the framework of the EUROfusion Consortium and has received funding from the Euratom research and training programme 2014-2018 and 2019-2020 under grant agreement No. 633053. The views and opinions expressed herein do not necessarily reflect those of the European Commission. The work of A. Froio is financially supported by a EUROfusion Engineering Grant.

Computational resources were provided by HPC@POLITO, a project of Academic Computing within the Department of Control and Computer Engineering at the Politecnico di Torino (http://www.hpc.polito.it).


## Appendix A. Validation on a simplified case

To check and validate the chosen models and solvers, as well as the meshing strategy, a simple natural convection case has been set up, to compare the computed Nusselt number $Nu$ with that given by available correlations.

A steady-state 2D model has been set up, characterized by a vertical parallel plate channel, according to the scheme in Fig. 13; the length of the channel has been chosen in order to have fully developed flow. In analogy with the case of the BB cooling, a pressure of 0 Pa gauge and a temperature of 26 °C are imposed as inlet and outlet boundary conditions, and a uniform heat flux of 100 W/m² is imposed on the walls. The resulting value of $Ra$, computed as

$$Ra = \frac{g\beta q''\delta^3}{k\nu\alpha} \tag{11}$$

since the wall heat flux $q''$ is imposed [22], is $Ra \cong 2 \times 10^4$, so the flow will be laminar. All models and solvers adopted here are the same as those reported in section 4 above.

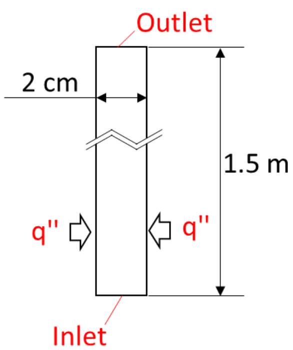


Fig. 13. Sketch of the 2D model used for the validation.

In the case of fully developed flow, the value of $Nu$ at channel outlet can be computed according to the experimental correlation [22]

$$Nu = 0.144\sqrt{Ra\frac{\delta}{L}} \tag{12}$$

where $L$ is the length of the channel. The corresponding heat transfer coefficient, considering as characteristic length the gap width, is equal to 4 W/(m² K).

Three different meshes have been adopted, which are shown in Fig. 14: "Mesh 1" is a fine unstructured polygonal mesh, and features ~10 cells in the channel width; "Mesh 2" is a coarse unstructured polygonal mesh, with ~4 cells in the channel width; "Mesh 3" is a structured rectangular mesh with 6 cells in the channel width. The most suitable meshing strategy for the 3D case will be chosen comparing this 2D result with correlation (12).

The results are reported in Fig. 14: both Mesh 1 and Mesh 3 give a $Nu$ value within 3 % from the correlation, which is nearly 1/3 of the deviation obtained with Mesh 2. Furthermore, a grid independence study on the number of layers shows that using 6 layers the error on the computed $Nu$ stays below 3 % with respect to a much more refined grid (24 layers), thus 6 layers are chosen to mesh the gap. This suggests that the models and solvers chosen as well as the meshing strategy for the gaps can be considered reliable also in the fully 3D problem, which is the 3D version of Mesh 3 (see Fig. 5c).

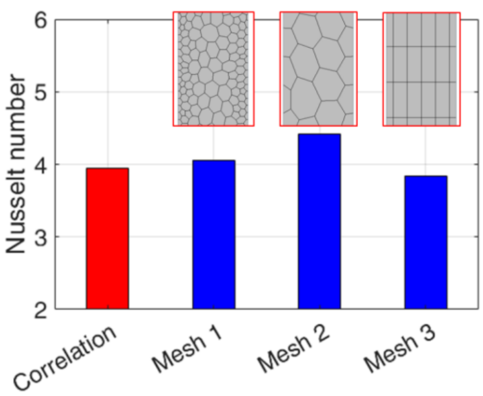


Fig. 14. Comparison of the $Nu$ obtained from the correlation (12) and numerically, with three different meshes.

## Appendix B. Material properties

In order to simplify the geometry (i.e. to avoid describing in detail the internals of the BB), the solid material of the BB segments is assumed homogeneous. The BB segments contain a mixture of EUROFER97 Reduced-Activation Ferritic-Martensitic steel (structural material), $Li_4SiO_4$ pebbles (breeder material), $Be_{12}Ti$ rods (neutron multiplier material), W (First Wall armour) and He (coolant). The volumes of the different materials in the IB, central OB (COB) and Left/Right OB (LOB/ROB) BB segments are reported in Table 1.

The properties are homogenised in order to conserve the total heat capacity and diffusivity of each segment; in addition, since the properties show a variation in the temperature range of interest (150÷400 °C) below 5 % [21], a constant, average value is assumed for the entire transient duration. The homogenised values are reported in Table 2.

To conserve the total mass of the solid object $M$, the density is a volume-averaged value, according to

$$M = \bar{\rho}V_{tot} = \sum_{i=1}^{N}\rho_i V_i \Rightarrow \bar{\rho} = \frac{\sum_{i=1}^{N}\rho_i V_i}{V_{tot}} \tag{13}$$

where $\bar{\rho}$ is the average density, $V_{tot} = \sum_{i=1}^{N} V_i$ is the total solid volume, $N = 5$ is the number of different materials in the BB segments, $\rho_i$ is the density of the $i$-th material, and $V_i$ is the volume of the $i$-th material.

To conserve the total heat capacity of the solid object $C$, the (mass) specific heat is a mass-averaged value, according to

$$C = M\bar{c} = \sum_{i=1}^{N}\rho_i c_i V_i \Rightarrow \bar{c} = \frac{\sum_{i=1}^{N}\rho_i c_i V_i}{M} \tag{14}$$

where $\bar{c}$ is the average specific heat and $c_i$ is the specific heat of the $i$-th material.

To conserve the heat diffusivity of the solid object, the thermal conductivity is a volume-averaged value, according to

$$\bar{k} = \frac{\sum_{i=1}^{N} k_i V_i}{V_{tot}} \tag{15}$$

where $\bar{k}$ is the average thermal conductivity and $k_i$ is the thermal conductivity of the $i$-th material.

Table 1. Volume of different materials in the HCPB BB [25].

| Material | COB | LOB/ROB | IB |
|---|---|---|---|
| EUROFER97 | 6.53 m³ | 6.20 m³ | 4.03 m³ |
| $Li_4SiO_4$ | 1.83 m³ | 1.74 m³ | 1.13 m³ |
| $Be_{12}Ti$ | 6.07 m³ | 5.76 m³ | 3.75 m³ |
| W | 0.047 m³ | 0.044 m³ | 0.029 m³ |
| He | 6.38 m³ | 6.06 m³ | 3.94 m³ |

## Appendix C. Space and time convergence studies

The choice of the grid size and timestep used in the work has been undertaken via convergence analyses; the quantity used for the analyses is the volume-averaged temperature in the solid domain after 13 ks (i.e. ~3.6 h) of transient $T_{solid}^{ave}$.

Table 2. Material properties in the HCPB BB.

| **Material** | ***k* [W/(m K)]** | ***c* [J/(kg K)]** | ***ρ* [kg/m³]** |
|---|---|---|---|
| EUROFER97 [21] | 25.2 | 574.0 | 7685 |
| $Li_4SiO_4$ [21] | 0.920 | 1789 | 1526 |
| $Be_{12}Ti$ [26] | 34.3 | 2384 | 3468 |
| W [27] | 149 | 139.0 | 19290 |
| He [28] | 0.249 | 5190 | 6.611 |
| Homogenised | 18.4 | 1143 | 3647 |

## Space convergence

Four different meshes are created, having a characteristic cell size of 0.5 m, 0.375 m, 0.25 m and 0.125 m, corresponding to a total cell count of ~402 thousands, ~691 thousands, ~1.60 million, and ~5.83 million, respectively. The values of $T_{solid}^{ave}$ for the different grids are reported in Fig. 15, together with the "exact" value estimated with the Richardson Extrapolation (RE) technique [29] (filled circle). For all the four grids, the error with respect to the exact value is <3.2 %, so the coarsest grid is chosen for the analysis

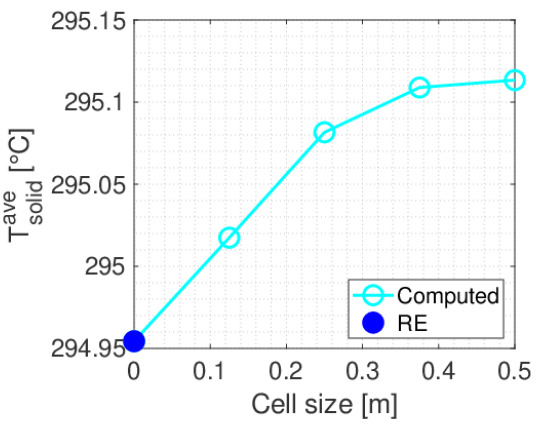


Fig. 15. $T_{solid}^{ave}$ for the different grids (empty circles) and "exact" value estimated with RE.

## Time convergence

Similarly to the space convergence study, five different time steps for the "solid" physics $\Delta t_{solid}$ have been used (0.25 s, 0.5 s, 1 s, 2 s and 4 s), keeping constant the $\Delta t_{fluid}/\Delta t_{solid}$ ratio (see section 3 above). The corresponding values of $T_{solid}^{ave}$ are reported in Fig. 16, together with the "exact" value estimated with the RE technique (filled circle). For $\Delta t_{solid} = 1$ s, an error of ~2.2 % is found, which is comparable to (and below) the value obtained for the space convergence, so 1 s is chosen as time step for the analysis.

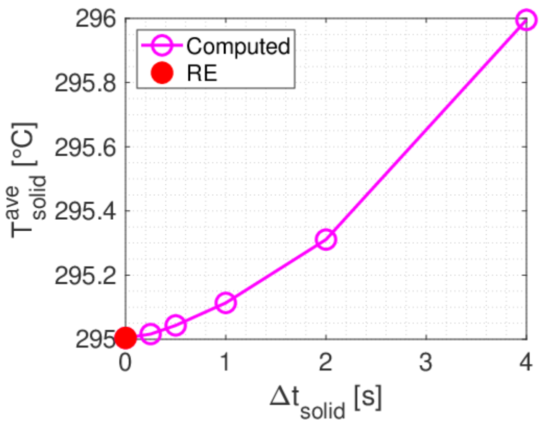


Fig. 16. $T_{solid}^{ave}$ for the different time steps (empty circles) and "exact" value estimated with RE.

## References


[1] A. J. H. Donné, W. Morris, X. Litaudon, C. Hidalgo, D. McDonald, H. Zohm, E. Diegele, A. Möslang, K. Nordlund, G. Federici, P. Sonato, C. Waldon, D. Borba and P. Helander, European research roadmap to the realisation of fusion energy, EUROfusion Consortium, 2018. [Online]. Available: https://www.euro-fusion.org/fileadmin/user_upload/EUROfusion/Documents/TopLevelRoadmap.pdf. [Accessed 2 June 2020].

[2] F. Cismondi, L. V. Boccaccini, G. Aiello, J. Aubert, C. Bachmann, T. Barrett, L. Barucca, E. Bubelis, S. Ciattaglia, A. Del Nevo, E. Diegele, M. Gasparotto, G. Di Gironimo, P. A. Di Maio, F. A. Hernández, G. Federici, I. Fernández-Berceruelo, T. Franke, A. Froio, C. Gliss, J. Keep, A. Loving, E. Martelli, F. Maviglia, I. Moscato, R. Mozzillo, Y. Poitevin, D. Rapisarda, L. Savoldi, A. Tarallo, M. Utili, L. Vala, G. Veres and R. Zanino, Progress in EU Breeding Blanket design and integration, Fusion Engineering and Design 136(A):782-792, 2018.

[3] G. A. Spagnuolo, G. Bongiovì, F. Franza and I. A. Maione, Systems Engineering approach in support to the breeding blanket design, Fusion Engineering and Design 146(A):31-35, 2019.

[4] G. A. Spagnuolo, L. V. Boccaccini, G. Bongiovì, F. Cismondi and I. A. Maione, Development of load specifications for the design of the breeding blanket system, Fusion Engineering and Design 157:111657, 2020.

[5] J. Keep, S. Wood, N. Gupta, M. Coleman and A. Loving, Remote handling of DEMO breeder blanket segments: Blanket transporter conceptual studies, Fusion Engineering and Design 124:420-425, 2017.
[6] Siemens, STAR-CCM+, 2019. [Online]. Available: https://www.plm.automation.siemens.com/global/it/products/simcenter/STAR-CCM.html. [Accessed 27 November 2019].
[7] D. Leichtle, P. Pereslavtsev, J. Sanzi, J. P. Catalan and R. Juarez, Global shutdown dose rate maps for a DEMO conceptual design, Fusion Engineering and Design 98-99:1524-1527, 2015.
[8] Y. Someya, H. Utoh, R. Hiwatari, H. Tanigawa, K. Tobita and the Joint Special Design Team for Fusion, Shutdown dose-rate assessment during the replacement of in-vessel components for a fusion DEMO reactor, Fusion Engineering and Design 124:615-618, 2017.
[9] B. Končar, M. Draksler, O. Costa Garrido and B. Meszaros, Thermal radiation analysis of DEMO tokamak, Fusion Engineering and Design 124:567-571, 2017.
[10] B. Končar, O. Costa Garrido M. Draksler, R. Brown and M. Coleman, Initial optimization of DEMO fusion reactor thermal shields by thermal analysis of its integrated systems, Fusion Engineering and Design 125:38-49, 2017.
[11] M. Draksler, B. Končar, M. Tekavčič and C. Bachmann, CFD analysis of the natural circulation of helium in the DEMO cryostat during a leak accident, Fusion Engineering and Design 158:111752, 2020.
[12] Siemens, STAR-CCM+ User's Manual, v2019.3.
[13] R. Wenninger, DEMO1 Reference Design – 2017 March ("EU DEMO1 2017"), EFDA_D_2NE9JA, 2017, unpublished.
[14] C. Gliss, June-2017 DEMO Reference Configuration model, EFDA_D_2N4EZW, 2017, unpublished.
[15] F. A. Hernández, P. Pereslavtsev, G. Zhou, B. Kiss, Q. Kang, H. Neuberger, V. Chakin, R. Gaisin, P. Vladimirov, L. V. Boccaccini, G. A. Spagnuolo, S. D'Amico and I. Moscato, Advancements in the Helium-Cooled Pebble Bed Breeding Blanket for the EU DEMO: Holistic Design Approach and Lessons Learned, Fusion Science and Technology 75(5):352-364, 2019.
[16] A. Del Nevo, P. Arena, G. Caruso, P. Chiovaro, P. A. Di Maio, M. Eboli, F. Edemetti, N. Forgione, R. Forte, A. Froio, F. Giannetti, G. Di Gironimo, K. Jiang, S. Liu, F. Moro, R. Mozzillo, L. Savoldi, A. Tarallo, M. Tarantino, A. Tassone, M. Utili, R. Villari, R. Zanino and E. Martelli, Recent progress in developing a feasible and integrated conceptual design of the WCLL BB in EUROfusion project, Fusion Engineering and Design 146(B):1805 1809, 2019.
[17] F. Cismondi, private communication, 2018.
[18] S. Irving, B. Fordand and D. Etheridge, Natural ventilation in non-domestic buildings, CIBSE Applications Manual AM10, 2005.
[19] C. Bachmann and F. Cismondi, private communication, Jan. 2019.
[20] T. Härtl, C. Bachmann, E. Diegele and G. Federici, Rationale for the selection of the operating temperature of the DEMO Vacuum Vessel, Fusion Engineering and Design 146:1096-1099, 2019.
[21] P. Frosi, IVC RM interface temperatures during shutdown, EFDA_D_2MAG8P, 2018, unpublished.
[22] F. Incropera and D. Dewitt, Fundamentals of heat and mass transfer, 7th edition, John Wiley & Sons, 2011.
[23] STAR-CCM+ User's Manual v14.06.
[24] [dataset] A. Zappatore and A. Froio, CFD analysis of natural convection cooling of the in-vessel components during a shutdown of the EU DEMO fusion reactor (dataset), Zenodo, v1.0.0, 2020, 10.5281/zenodo.3922265.
[25] F. A. Hernández, P. Pereslavtsev, G. Zhou, Q. Kang, S. D'Amico, A. Retheesh and H. Neuburger, HCPB design and integration studies 2019, EFDA_D_2NKC7G, 2020, unpublished.
[26] M. Uchida, E. Ishitzuka and H. Kawamura, Thermal conductivity of neutron irradiated $Be_{12}Ti$, Fusion Engineering and Design 69(1-4):499-503, 2003.
[27] M. Fukuda, A. Hasegawa and S. Nogami, Thermal properties of pure tungsten and its alloys for fusion applications, Fusion Engineering and Design 132:1-6, 2018.
[28] E. W. Lemmon, M. L. Huber and M. O. McLinden, Reference Fluid Thermodynamic and Transport Properties, NIST Standard Reference Database 23, version 9.1, 2013.
[29] P. J. Roache, Verification and validation in computational science and engineering; Hermosa Publishers, Albuquerque, NM, USA, 1998.